Chapter 6

An analytical viscous model for atmospheric vortices with a central depression of pressure

6.1 Introduction

Atmospheric vortices, such as dust devils, tornadoes, and tropical cyclones, are aerial columns formed due to a regional temperature gradient. These vortices share similar fundamental dynamics, but their behaviour varies depending on environmental conditions. One of the essential features of these vortices is the central region of low-pressure, which plays an important role in the genesis and sustainability of the vortex structure. The main objective of modelling these vortices is to comprehend how this low-pressure area forms and further impacts vortex dynamics. Recent developments demonstrate the low-pressure

core's crucial role in determining vortex behaviour, especially when it comes to its interactions with the surrounding flow and boundary layer (Kepert (2001); Balme and Greeley (2006a); Giersch and Raasch (2023)).

Research on atmospheric vortices has been ongoing for over a hundred years. Much of the early research on dust devils and tornado-like vortices focused on how air rises and rotates due to surface heating and the ensuing atmospheric instability. While Smith and Leslie (1976) investigated the atmospheric conditions necessary for the development of vortex flow, early models by Sinclair (1973) concentrated on the role of surface heating in dust devil formation.

SHAPIRO (1982) investigated the relationship between hurricane frequency and intensity variability and large-scale atmospheric circulation patterns in tropical cyclones. The study emphasised how long-term variations in tropical cyclone activity are influenced by synoptic-scale factors. Rogers et al. (2020) investigated the dynamics of dust devils and tornado-like vortices by incorporating both radial and axial velocity components, extending earlier models. Onishchenko et al. (2021b) demonstrated that inner-core dynamics, including the low-pressure centre, critically influence wind structure and cyclone development under moderate vertical shear using high-resolution simulations.

Additionally, boundary layer effects have proved important in modifying the behaviour of vortices. The impact of viscosity in altering vortex flow close to the surface, especially in high Reynolds-number flows as those in dust devils, was investigated by Sullivan (1959). More recently, Giersch and Raasch (2023) investigated the boundary layer dynamics in dust devils using large-eddy simulations (LES), confirming that the boundary layer has a major impact on the low-pressure zone, which is essential for the creation and stability of vortices.

Farrell et al. (2003c, 2004, 2006) examined the roles of electromagnetic forces in dust devil dynamics and proposed that electric fields are a minor but significant factor in vortex formation. These forces affect how dust particles and air interact, which helps to maintain the stability as well as the longevity of vortices. This theory has been supported by laboratory studies, such as those by Melnik and Parrot (1998), Zhou et al. (2002), Zheng et al. (2003), and Xie et al. (2007), which confirmed that the interaction of charged particles with airflow can enhance vortex behaviour. Additionally, studies by Harrison et al. (2016) and Izvekova and Popel (2016, 2017, 2020) have shown that electric forces play a role in dust devil formation, both on Earth and Mars.

The dynamics of vortex development generally follow three stages, viz. formation, quasi-stationary state, and decay. Much research has focused on understanding the initial formation of vortices. Notable works, such as those by Kanak (2005), Rennó et al. (1998), and Onishchenko et al. (2015), have modelled the formation phase, but a gap remains in fully capturing the complexity of vortex transition from an incipient to a fully developed state.

One of the key aspects that has been explored in recent work is the central low-pressure zone in vortices. Onishchenko et al. (2021b) introduced a model that incorporates both radial and axial velocity components and pressure distributions. Their model highlights the importance of low-pressure region in maintaining the vortex's strength and structure. According to Pandey and Maurya (2017), a dust devil cannot form or survive without a low-pressure zone, and the vortex's survival depends on the persistence of this low-pressure region.

The importance of the low-pressure zone in vortex dynamics has been highlighted by recent theoretical contributions. A generalised analytical viscous model was presented by Yadav et al. (2024) to explain the steady-state behaviour of atmospheric vortices. To accurately depict the impact of viscosity on vortex structure, it included both

axial and radial variations. Likewise, Pandey and Yadav (2024) created a mathematical model for tropical cyclone viscous flow dynamics, emphasising how the low-pressure zone affects cyclone intensification. According to their research, stronger cyclonic winds and more severe storms are caused by the deepening of the low-pressure core. Giersch and Raasch (2023) investigated how dust devil-like vortices are influenced by model resolution through a grid convergence study using large-eddy simulations. Their results highlighted the importance of fine spatial resolution for accurately capturing vortex structure and intensity. Finally, Rogers et al. (2020) analysed the role of precipitation processes and vortex alignment in the intensification of a weak tropical cyclone under moderate vertical wind shear. According to their research, cyclone strengthening is facilitated by vertical coherence and convective structure.

In conclusion, recent improvements in the study of atmospheric vortices indicate that the low-pressure zone is an essential part of both small and large-scale vortices. Research emphasises how the low-pressure zone affects the formation, development, intensification, and growth of vortices. Even though there has been a lot of progress, more work is needed to fully understand the complexity of vortex dynamics, particularly when it comes to boundary layer impacts and environmental variables. As a result, a key component of vortex dynamics is pressure depression. This work aims to further enhance an existing model by adding a low-pressure area to generalised fluid motion given by Yadav et al. (2024).

6.2 Mathematical Formulation of the Problem

We examine a steady, axi-symmetric atmospheric vortex described in cylindrical polar coordinates $(\tilde{r}, \tilde{\theta}, \tilde{z})$, where $\tilde{r}$, $\tilde{\theta}$, and $\tilde{z}$ represent the radial, azimuthal, and vertical coordinates, respectively. In the present model, we consider the flow to be both viscous and

incompressible, with the assumption that the vortex rotates symmetrically about the vertical axis. The governing equations for the motion of this incompressible viscous fluid are given by

$$\left(\tilde{u}\frac{\partial\tilde{u}}{\partial\tilde{r}}+\tilde{w}\frac{\partial\tilde{u}}{\partial\tilde{z}}-\frac{\tilde{v}^2}{\tilde{r}}\right)=-\frac{1}{\rho}\frac{\partial\tilde{p}}{\partial\tilde{r}}+\nu\left(\frac{\partial^2\tilde{u}}{\partial\tilde{r}^2}+\frac{1}{\tilde{r}}\frac{\partial\tilde{u}}{\partial\tilde{r}}-\frac{\tilde{u}}{\tilde{r}^2}+\frac{\partial^2\tilde{u}}{\partial\tilde{z}^2}\right), \tag{6.1}$$

$$\left(\tilde{u}\frac{\partial\tilde{v}}{\partial\tilde{r}}+\tilde{w}\frac{\partial\tilde{v}}{\partial\tilde{z}}+\frac{\tilde{u}\tilde{v}}{\tilde{r}}\right)=\nu\left(\frac{\partial^2\tilde{v}}{\partial\tilde{r}^2}+\frac{1}{\tilde{r}}\frac{\partial\tilde{v}}{\partial\tilde{r}}-\frac{\tilde{v}}{\tilde{r}^2}+\frac{\partial^2\tilde{v}}{\partial\tilde{z}^2}\right), \tag{6.2}$$

$$\left(\tilde{u}\frac{\partial\tilde{w}}{\partial\tilde{r}}+\tilde{w}\frac{\partial\tilde{w}}{\partial\tilde{z}}\right)=-\frac{1}{\rho}\frac{\partial\tilde{p}}{\partial\tilde{z}}+\nu\left(\frac{\partial^2\tilde{w}}{\partial\tilde{r}^2}+\frac{1}{\tilde{r}}\frac{\partial\tilde{w}}{\partial\tilde{r}}+\frac{\partial^2\tilde{w}}{\partial\tilde{z}^2}\right), \tag{6.3}$$

together with the continuity equation

$$\frac{1}{\tilde{r}}\frac{\partial(\tilde{r}\tilde{u})}{\partial\tilde{r}}+\frac{\partial\tilde{w}}{\partial\tilde{z}}=0, \tag{6.4}$$

where $\tilde{u}$, $\tilde{v}$, $\tilde{w}$, ν stand for the radial, azimuthal, and axial velocity components, and the kinematic viscosity, respectively. Additionally, $\tilde{p}$ is pressure.

To ensure dynamical similarity, we reduce the governing equations (6.1–6.4) with the following dimensionless variables

$$r=\frac{\tilde{r}}{r_m},\quad z=\frac{\tilde{z}}{r_m},\quad u=\frac{\tilde{u}}{v_m},\quad v=\frac{\tilde{v}}{v_m},\quad w=\frac{\tilde{w}}{v_m},\quad p=\frac{\tilde{p}}{\rho v_m^2},$$

v_m being the maximum azimuthal velocity at the radius r_m, to

$$u\frac{\partial u}{\partial r}+w\frac{\partial u}{\partial z}-\frac{v^2}{r}=-\frac{\partial p}{\partial r}+\frac{1}{Re}\left(\frac{\partial^2 u}{\partial r^2}+\frac{1}{r}\frac{\partial u}{\partial r}+\frac{\partial^2 u}{\partial z^2}-\frac{u}{r^2}\right), \tag{6.5}$$

$$u\frac{\partial v}{\partial r}+w\frac{\partial v}{\partial z}+\frac{uv}{r}=\frac{1}{Re}\left(\frac{\partial^2 v}{\partial r^2}+\frac{1}{r}\frac{\partial v}{\partial r}+\frac{\partial^2 v}{\partial z^2}-\frac{v}{r^2}\right), \tag{6.6}$$

$$u\frac{\partial w}{\partial r}+w\frac{\partial w}{\partial z}=-\frac{\partial p}{\partial z}+\frac{1}{Re}\left(\frac{\partial^2 w}{\partial r^2}+\frac{1}{r}\frac{\partial w}{\partial r}+\frac{\partial^2 w}{\partial z^2}\right), \tag{6.7}$$

$$\frac{1}{r}\frac{\partial(ru)}{\partial r}+\frac{\partial w}{\partial z}=0, \tag{6.8}$$

where $Re=\frac{v_m r_m}{\nu}$ denotes the Reynolds number.

6.3 Empirical Consideration of Stream-Function

Onishchenko et al. (2021b) concluded that maximum axial velocity is attained at the central axis. However unlike their inference, maximum axial velocity occurs somewhat away from the axis and near the periphery of the centrally placed low pressure area (see Pandey and Maurya (2017), Yadav et al. (2024) etc.). This requires a modification in the stream function. This is achieved by a slight modification in that given by Onishchenko et al. (2021b) to the form

$$\psi=\beta r(r-c)ze^{-z-(r-c)^2}, \tag{6.9}$$

where r, z is the radial, the vertical coordinate respectively and c is the radius of the central low-pressure zone often referred to as the core of the vortex.

6.4 Analysis

Using the Stokes stream-function ψ, we determine the velocity components in the radial and vertical directions through

$$u=-\frac{1}{r}\frac{\partial\psi}{\partial z} \quad \text{and} \quad w=\frac{1}{r}\frac{\partial\psi}{\partial r}. \tag{6.10}$$

Substituting ψ in Eq.(10), we can derive the velocity components

$$u=-\beta\,(r-c)\,(1-z)\,e^{-z-(r-c)^2}, \tag{6.11}$$

$$w = \beta\, z\, \frac{(2r - c) - 2r(r - c)^2}{r}\, e^{-z-(r-c)^2}. \tag{6.12}$$

To determine β, we use an observed or imposed boundary condition. Suppose that the radial velocity reaches a known maximum value $u_{\max}$ at a given point (r_0, z_0). Then, the constant β can be obtained as

$$\beta = \frac{-u_{\max}}{(r_0 - c)(1 - z_0)e^{-z_0-(r_0-c)^2}}.$$

We aim to solve for the azimuthal velocity $v(r, z)$ for inviscid flow using Eq.(6.6)

$$u\frac{\partial v}{\partial r} + w\frac{\partial v}{\partial z} + \frac{uv}{r} = 0. \tag{6.13}$$

Assuming conservation of angular momentum in axisymmetric inviscid flow, we set $M = rv =$ constant along streamlines, which implies

$$v(r, z) = \frac{f(\psi)}{r}, \tag{6.14}$$

where f is an arbitrary function of the stream-function ψ. Using the expression for ψ from Eq. (6.9), we write:

$$v(r, z) = \frac{f\left(\beta\, r(r - c)\, z\, e^{-z-(r-c)^2}\right)}{r} \tag{6.15}$$

Assuming a power-law form for $f(\psi) = A\psi^k$, we obtain

$$\begin{aligned} v(r, z) &= \frac{A}{r}\left[\beta\, r(r - c)\, z\, e^{-z-(r-c)^2}\right]^k, \\ &= A\,\beta^k\, r^{k-1}\,(r - c)^k\, z^k\, e^{-kz-k(r-c)^2}. \end{aligned} \tag{6.16}$$

The inviscid solution for the azimuthal velocity, derived from the azimuthal momentum equation, does not satisfy the no-slip condition at $z = 0$, as it neglects the viscous effects near the surface. To enforce $v(r, 0) = 0$ at the boundary, a correction term is introduced.

At higher z, this correction makes sure that the velocity is zero at the ground and smoothly transitions to the inviscid solution.

The no-slip criterion is not physically enforced, but rather a mathematical coincidence, even if the inviscid solution v technically fulfils $v(r,0) = 0$ because of the factor z^k (for $k > 0$). Atmospheric vortices occur at high Reynolds numbers ($Re \gg 1000$), where viscous effects are confined to a thin boundary layer near the ground. This correction is usually based on how thin the boundary layer is near the surface.

The inviscid solution does not satisfy the no-slip condition in a viscous flow. For $k > 0$, $z^k = 0$ at $z = 0$, so $v(r,0) = 0$, but this is a mathematical artifact rather than a physical no-slip condition enforced by viscosity. Atmospheric vortices exist at high Reynolds numbers ($Re \gg 10000$), where viscous effects are significant only in a thin boundary layer near the ground ($z = 0$).

For high Re, viscous effects are confined to a boundary layer of thickness $\delta \sim \frac{1}{\sqrt{Re}}$. To capture this, we introduce a stretched coordinate

$$\zeta = z\sqrt{Re}. \tag{6.17}$$

This scales the vertical coordinate so that the viscous term becomes significant.

$$\frac{\partial v}{\partial z} = \frac{\partial v}{\partial \zeta} \cdot \sqrt{Re}, \quad \frac{\partial^2 v}{\partial z^2} = \frac{\partial}{\partial z}\left(\sqrt{Re}\frac{\partial v}{\partial \zeta}\right) = \sqrt{Re} \cdot \frac{\partial}{\partial \zeta}\left(\frac{\partial v}{\partial \zeta}\right) \cdot \sqrt{Re} = Re\frac{\partial^2 v}{\partial \zeta^2}. \tag{6.18}$$

This makes the viscous term order 1 in the boundary layer, balancing convective terms.

In boundary layer theory , the velocity transitions from zero at the boundary to the outer flow via an exponential function. We propose the following form

$$v_{visc} = v \cdot f(\zeta), \quad \zeta = z\sqrt{Re},$$

where $f(\zeta)$ satisfies $f(0) = 0$ to enforce $v_{visc}(r, 0) = 0$. $f(\zeta) \to 1$ as $\zeta \to \infty$ to recover v. A simple function is

$$f(\zeta) = 1 - e^{-\zeta} = 1 - e^{-z\sqrt{Re}}. \tag{6.19}$$

Thus, the corrected velocity profile becomes

$$v_{visc}(r, z) = v \cdot \left(1 - e^{-z\sqrt{Re}}\right) = A\,\beta^k\, r^{k-1}\,(r-c)^k\, z^k\, e^{-kz-k(r-c)^2} \left(1 - e^{-z\sqrt{Re}}\right). \tag{6.20}$$

This correction ensures that the velocity profile satisfies the no-slip condition at the ground and transitions smoothly to the inviscid flow at higher heights, where the viscous effects become negligible. In view of Eq.(6.1) and Eq.(6.3), we have derived pressure $p(r, z)$ for inviscid flow as

$$p(r, z) = p(c, 0) - \left(\frac{u^2 + w^2}{2}\right) + \int_c^r \frac{v^2}{r}\, dr - \int_0^z u\frac{\partial w}{\partial r}\, dz - \int_c^r w\frac{\partial u}{\partial z}\, dr, \tag{6.21}$$

$$\begin{aligned} p(r, z) = p(c, 0) &- \frac{1}{2}\left[\beta^2(r-c)^2(1-z)^2 + \beta^2 z^2 \left(\frac{(2r-c) - 2r(r-c)^2}{r}\right)^2\right] e^{-2z-2(r-c)^2} \\ &+ \int_c^r \frac{A^2\beta^2(s-c)^2 z^2 e^{-2z-2(s-c)^2}}{s}\, ds \\ &+ \beta^2 \int_0^z (r-c)(1-z')e^{-z'-(r-c)^2} \cdot \frac{\partial}{\partial r}\left[z' \frac{(2r-c) - 2r(r-c)^2}{r} e^{-z'-(r-c)^2}\right] dz' \\ &+ \beta^2 \int_c^r z \frac{(2s-c) - 2s(s-c)^2}{s} e^{-z-(s-c)^2} \cdot (s-c)(1-z)e^{-z-(s-c)^2}\, ds \end{aligned} \tag{6.22}$$

6.5 Results and Discussion

6.5.1 Radial velocity

Fig. (6.1) illustrates the radial profiles of the radial velocity that is derived from Eq. (6.10), across various heights, with each subplot containing three curves corresponding to different z values. At lower altitudes ($z < 1$), as Fig. (6.1a) shows, the wind is directed toward the axis, indicating an inflow from the outer regions. The radial velocity is negative due to its inward direction. It increases in magnitude radially inward, reaching a maximum at $r \approx c+1/\sqrt{2} \approx c+0.707$ for all curves. Beyond this point, the velocity decreases in magnitude and approaches zero at the periphery of the low-pressure zone. For heights above $z = 1$, an outflow is observed. In the range $1 < z < 2$ in Fig. (6.1b), the radial velocity increases with height across the curves, while it decreases for $z > 2$, compatible with the formula in Eq. (6.11) in Fig. (6.1c). These variations highlight the height-dependent dynamics of the radial flow, with the maximum inflow occurring at a consistent height beyond which outflow is observed.

Fig. (6.2) shows the variation of the low-pressure zone for radial velocity along radius. We observe that the maximum radial velocity moves away from the low-pressure zone as c increases.

6.5.2 Axial velocity

Fig. (6.3) shows the non-dimensionalised axial velocity, based on Eq. (6.12), along r for different heights with $c = 0.3$. The vertical velocity attains its maximum near the periphery of a low-pressure zone. As r increases further, w decreases and eventually becomes negative, indicating regions beyond the vortex's effective influence. In Fig. (6.3a), w

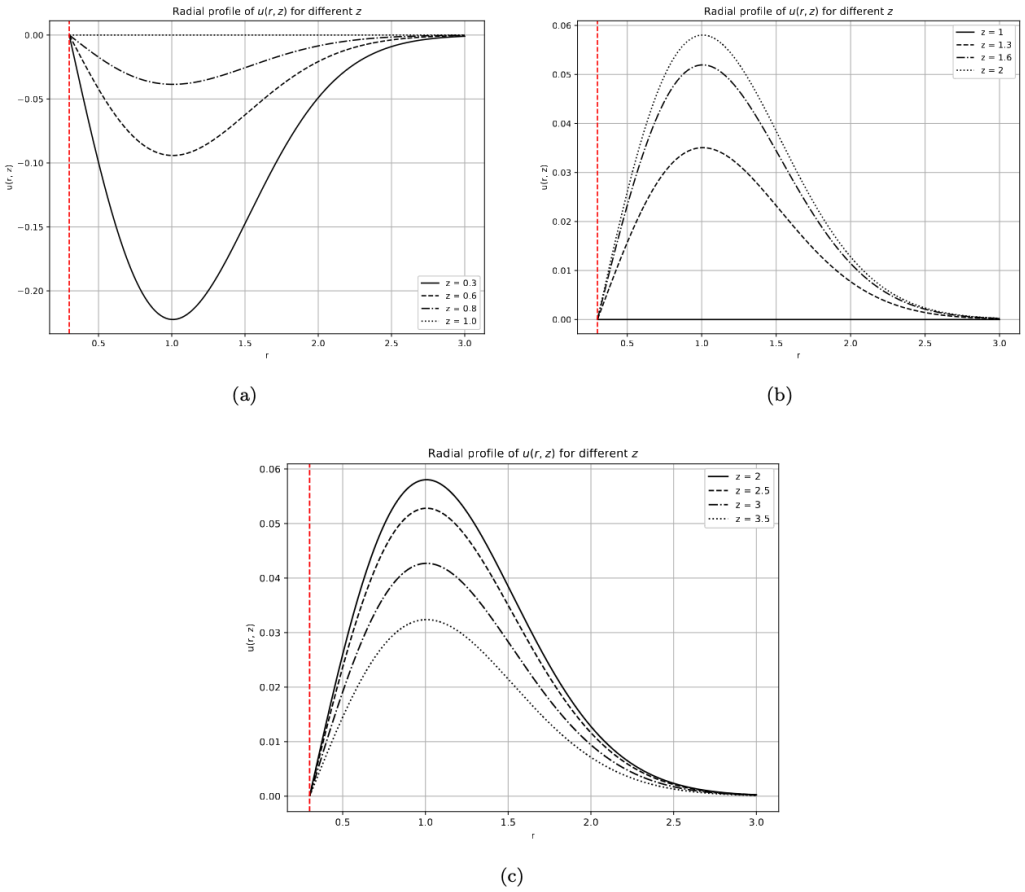

Figure 6.1: Plots (a)-(b) represent the radial profile of the non-dimensionalised radial velocity for $z \leq 1$ and $z \geq 1$, respectively. The other parameters being $c = 0.3$.

intensifies with height for $0 < z < 1$, whereas in Fig. (6.3b) it weakens as z increases. This indicates that the radial extent of the vertical motion is determined by c, and it also represents a larger vertical updraft near the surface that tapers off with height.

Fig. (6.4) shows the vertical velocity of a dust devil along the radius for different values of c, where the parameter c represents the size of the low-pressure region of the dust devil. Smaller c values correspond to a smaller low-pressure region, leading to higher peak vertical velocities closer to the centre. As c increases, resulting in lower peak velocities and a more spread-out velocity profile. This indicates that a smaller low-pressure region drives more intense vertical flow near the dust devil's centre, while a larger low-pressure

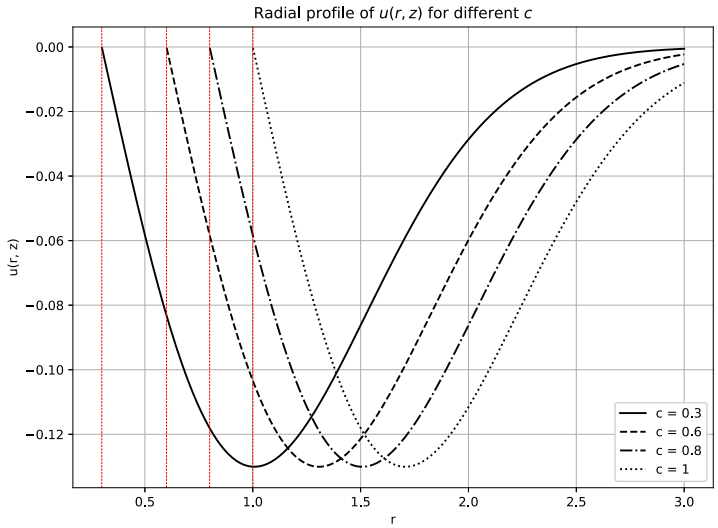

Figure 6.2: The graphs show the radial velocity (u) along the radial distance (r) for different c.

region leads to a more uniform flow over a larger radius.

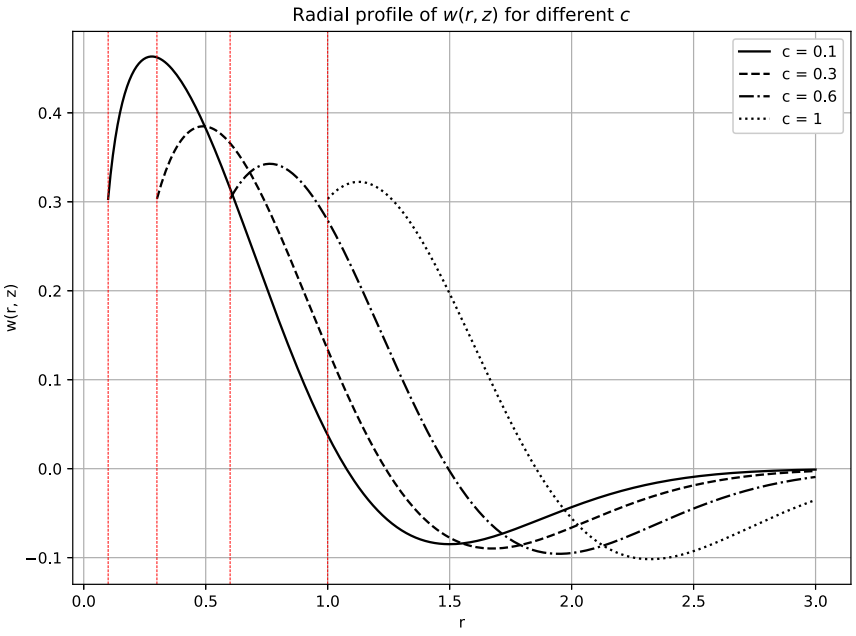

Figure 6.4: The graphs show the axial velocity (w) along the radial distance (r) for different c.

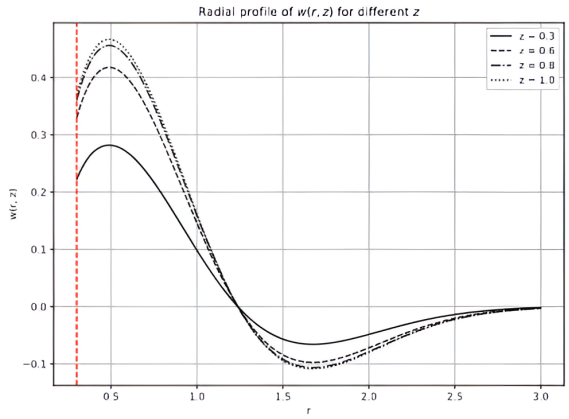

(a)

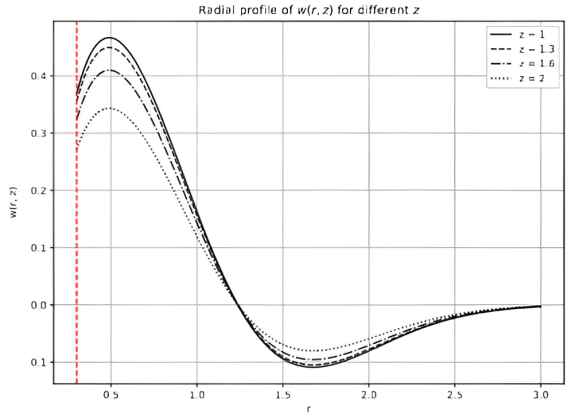

(b)

Figure 6.3: Plots (a)-(b) represent the radial profile of the non-dimensionalised axial velocity for $z \leq 1$, and $z > 1$ respectively. The other parameters being $c = 0.3$.

6.5.3 Azimuthal Velocity

Fig. (6.5) illustrates the radial variation of the azimuthal velocity, computed analytically with viscous correction. The azimuthal velocity profile exhibits key dynamical features of atmospheric vortices and highlights the role of model parameters in shaping the vortex structure.

At fixed height, the velocity rises from zero near the core ($r = c$), reaches a peak around the periphery of the low-pressure zone, and then decays rapidly to zero as r increases. Unlike models such as those by Baker and Sterling (2017) and Yadav

et al. (2024), where the azimuthal velocity decays asymptotically with radial distance, our model confines rotational motion within a finite radial extent. This behaviour more accurately reflects the nature of atmospheric vortices, which are typically compact and narrow, exhibiting limited radial expansion.

The azimuthal velocity exhibits strong height dependence. In the lower region ($0 < z \leq 1$), the peak of v increases with z, indicating intensification of rotational flow as the air ascends from the surface. At $z = 1$, the velocity reaches its maximum amplitude. For $z > 1$, however, the profile weakens with increasing height, reflecting the vertical decay of vortex strength.

Fig. (6.6) shows the effect of Reynolds number on the viscous azimuthal velocity profile. At fixed height $z = 0.1$, increasing Re sharpens the peak of v and intensifies the core rotation. For $Re = 10$, the velocity rises smoothly, while for $Re = 10000$, it increases steeply near $r = c$ before declining rapidly. This confirms the presence of a thin boundary layer at high Re, where viscosity dominates near the surface but becomes negligible at greater heights.

Fig. (6.7) explores the influence of the model parameter k on the velocity distribution. As k increases, the peak magnitude of v decreases, and the profile becomes broader and flatter. Lower values of k result in tightly confined, intense vortices, whereas higher k values produce weaker, more diffused rotational fields. This behaviour underscores the flexible nature of the model, allowing it to represent both intense atmospheric vortices and weaker convective vortices depending on environmental circumstances.

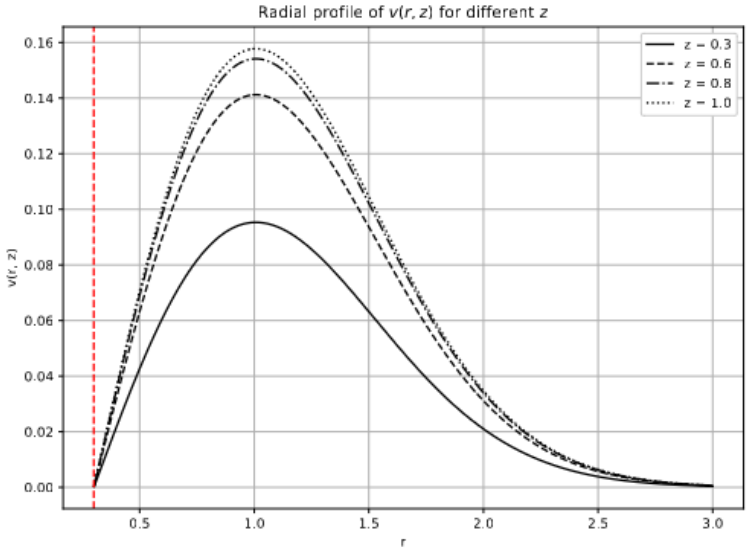

(a)

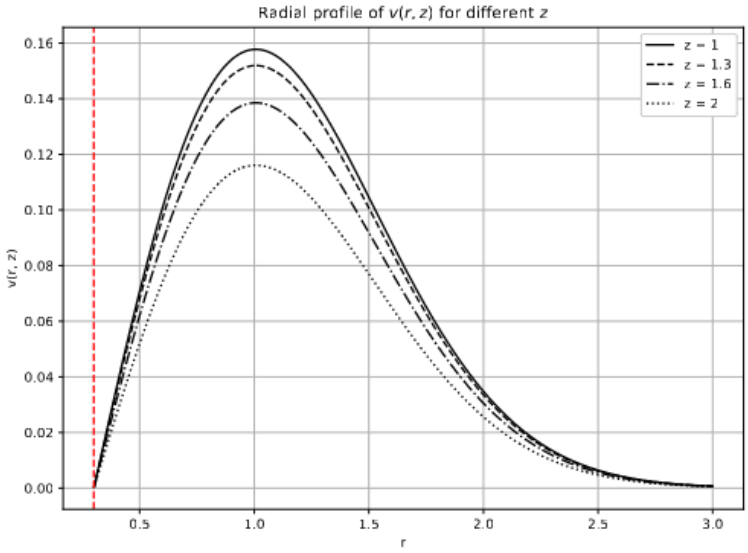

(b)

Figure 6.5: Plots (a) and (b) represent the radial profile of the non-dimensionalised azimuthal velocity for $z \leq 1$ and $z \geq 1$, respectively, with the parameter $c = 0.3$.

Fig. (6.8) reveal the impact of low pressure on azimuthal velocity. For all the low pressure region $c = 0.2 - 0.8$, the curves are symmetrical and we can also observe maximum azimuthal velocity is increasing with the size low pressure zone.

The azimuthal velocity field in this model captures essential features of dust devil dynamics such as finite radial extent of rotation, vertical modulation of rotational intensity, sensitivity to Reynolds number and structural parameter k.

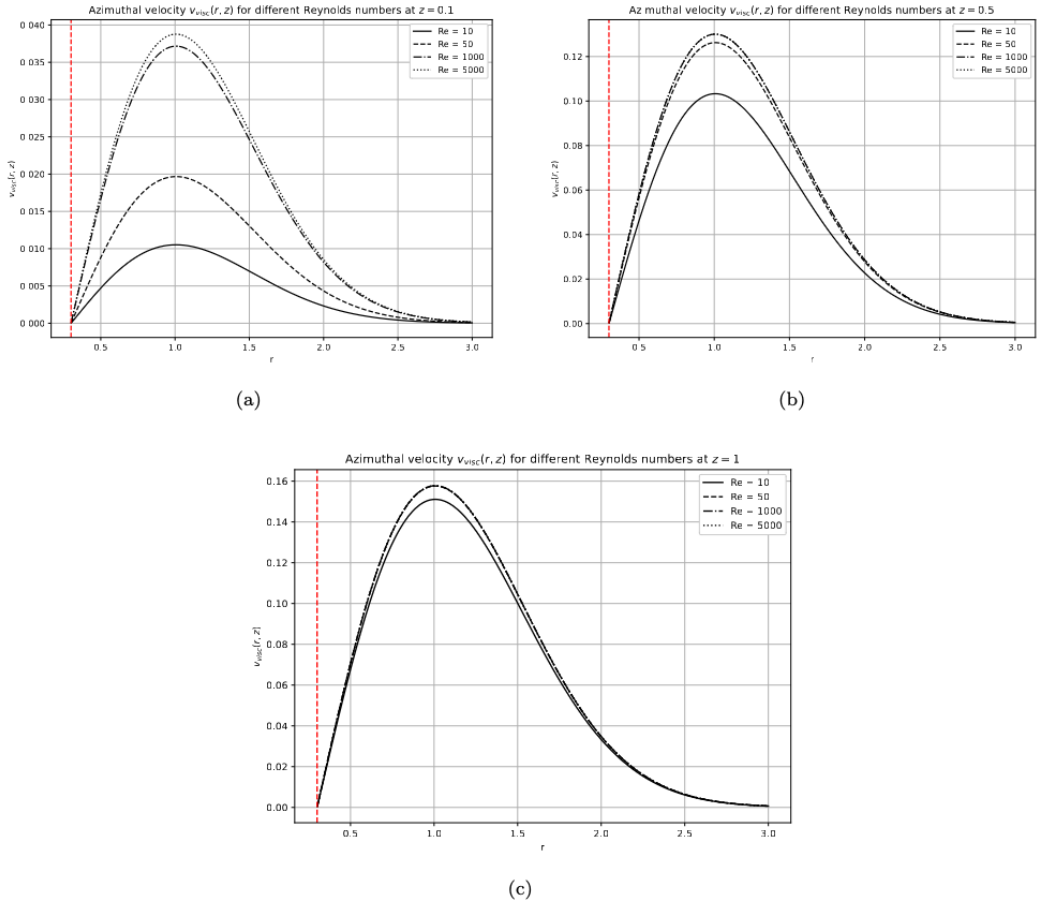

Figure 6.6: Plots (a)-(c) represent the radial profile of the non-dimensionalised viscous azimuthal velocity different Reynolds numbers. The other parameters being $c = 0.3$.

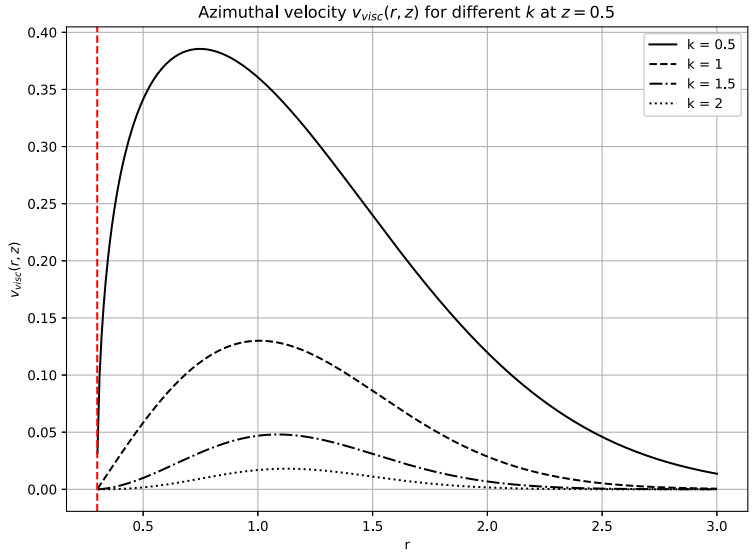

Figure 6.7: Radial profile of the non-dimensionalised azimuthal velocity for different values of k, with parameters $c = 0.3$ and $z = 1$.

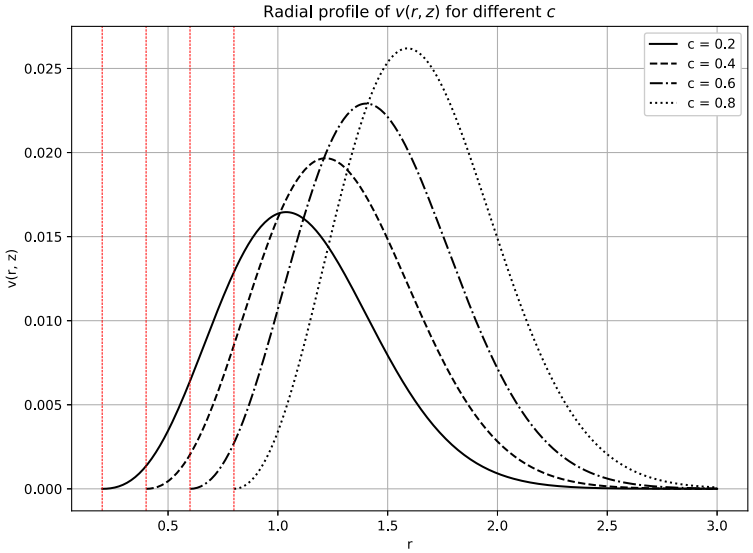

Figure 6.8: Azimuthal velocity (v) along the radial distance (r) for different values of c, with $z = 1$.

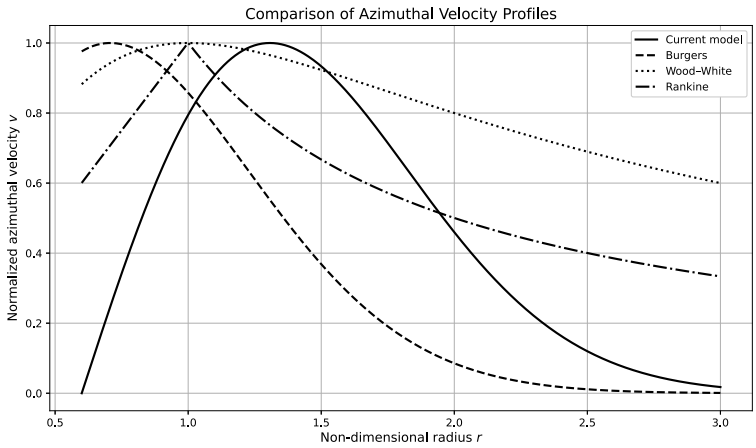

Figure 6.9: Comparison of the radial profile of the azimuthal velocity for the Rankine, Wood-White, Burgers, and current models, with parameters $c = 0.6$ and $z = 1$.

The present model offers significant improvements in capturing the realistic structure of atmospheric vortices when compared to existing models such as those of Rankine (1882), Burgers (1948), and Wood et al. (2013) in Fig. (6.9). Despite its mathematical simplicity and smoothness, the Burgers vortex does not restrict the swirl and assumes infinite radial decay. The velocity gradient at the core boundary of the Rankine (1882) vortex is discontinuous and does not physically continue. The Wood et al. (2013) model allows rotational motion over a wide radial region despite being continuous and flexible. In contrast, the azimuthal velocity in this model vanishes at a finite radius, better representing the compact rotation zone observed in field measurements. Additionally, the inclusion of a viscous correction enforces the no-slip boundary condition at the ground—an aspect inherently absent in inviscid models. The adjustable parameter k adds further flexibility, enabling the model to represent a range of vortex intensities and core sharpness. Collectively, these features allow our formulation to capture the localized and vertically stratified dynamics of atmospheric vortices with greater physical consistency with observations.

6.5.4 Pressure Distribution

Fig. (6.10) illustrates the radial variation of the radial pressure difference at various heights. At lower altitudes ($0 < z < 1$), as shown in Fig. (6.10a), the pressure increases sharply from the low-pressure core near $r = c$, reaches a maximum, then drops, and eventually flattens to an constant value as the radius increases. Convective vortices, such as dust devils, are characterised by significant radial inflow driven by a concentrated low-pressure zone, which is indicated by this sharp gradient.

In contrast, Fig.(6.10b) displays the pressure profiles for higher elevations ($1 \leq z \leq 4$). While the overall pattern remains consistent—rising pressure with radial distance—the gradient weakens with height. At $z = 1$, the pressure rise is still noticeable, but by $z = 3$, the profile becomes significantly flatter.

These trends indicate that the pressure distribution is more concentrated near the vortex core at lower heights, while at higher heights, the pressure field becomes more diffuse, reflecting the vertical structure of the dust devil where rotational effects weaken with increasing height.

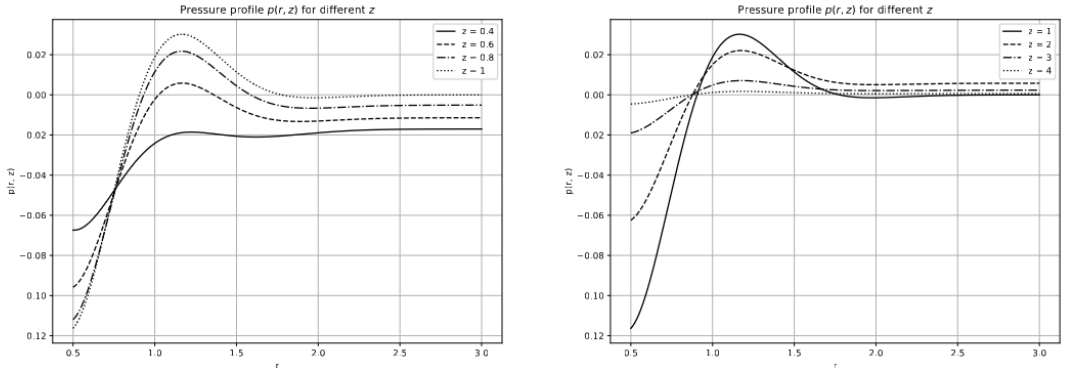

(a) (b)

Figure 6.10: Plots (a)-(b) represent the radial profile of the non-dimensionalised pressure for $z \leq 1$, and $z > 1$ respectively. The other parameters being $c = 0.3$.

6.6 Conclusion

This study presents a comprehensive analytical model for atmospheric vortices that incorporates all three components of the velocity field along with a pressure distribution derived from the momentum equations. The model introduces a generalized stream function and a viscous correction to the azimuthal velocity, enabling the velocity field to satisfy the no-slip condition at the ground while preserving the inviscid behaviour valid.

A key feature of the present model is the confinement of azimuthal velocity within a finite radial domain, unlike classical models such as Burgers (1948), Vatistas et al. (1986), Wood and Brown (2011), which extend the azimuthal velocity asymptotically to infinity. This leads to a more realistic representation of the compact structure of atmospheric vortices. The vertical decay in velocity and pressure fields captures the strong near-surface intensity and its weakening with height, consistent with field observations Sinclair (1973); Kanak (2005).

The sensitivity of the vortex structure to Reynolds number and model parameter offers flexibility in modelling both intense and weak vortices. Additionally, the model successfully captures key dynamical features such as inflow-outflow transitions, updraft localization, and the role of the central low-pressure zone in driving rotation and convergence.

****